FRONT CURVATURE RATE STICK MEASUREMENTS AND DETONATION SHOCK DYNAMICS CALIBRATION FOR PBX 9502 OVER A WIDE TEMPERATURE RANGE

L.G. Hill, J.B. Bdzil, T.D. Aslam
Los Alamos National Laboratory
Los Alamos, NM 87545

Detonation velocities and wave shapes were measured for PBX 9502 (95 wt.% TATB, 5 wt.% Kel-F 800) rate sticks at the temperatures -55, 25, and 75 C. At each initial temperature T_0 three diameters were fired: 50 mm, 18 mm, and 8, 10, and 12 mm respectively for the hot, ambient, and cold sticks. Wave shape data were fit with an analytic form, and the fitting parameters are listed along with thermal expansion and diameter effect data. For each T_0, the simplest detonation shock dynamics model assumes that the local normal wave speed D_n depends only on the local total curvature κ. The data confirm this notion for small κ, but curves for different charge diameters diverge at large κ. For each charge diameter, waves propagated more ideally in hotter charges than colder ones. For each T_0 a single best $D_n(\kappa)$ curve was found by global optimization. From these a $D_n(\kappa, T_0)$ calibration surface was generated to allow computation of problems with temperature gradients.

INTRODUCTION

Wave shape and detonation velocity data for rate sticks of differing diameters and initial temperatures is generally useful in validating detonation models. In the case of detonation shock dynamics (DSD) the role of such data is fundamental: one calibrates the model in a simple geometry, then infers by computation propagation in arbitrary geometries. Employing an experimental calibration allows DSD to bypass poorly understood issues such as reaction chemistry. It is also computationally efficient because it does not require calculation of the reaction zone structure.[1]

TATB is a natural material to start with because of its insensitivity. For a given curvature, a detonation wave in an insensitive heterogeneous explosive suffers a larger velocity deficit than does one in a traditional explosive. Thus, the need for a DSD approach (as opposed to Huygens' construction) is greater for such materials. The purpose of the present study is two-fold: to provide a general data set to test detonation propagation models, and to calibrate the simplest DSD model for PBX 9502 over a wide temperature range.

EXPERIMENT

DSD is an approximation to the Euler equations, which in its simplest form employs a function relating the local normal wave speed D_n to the local total curvature κ. Both quantities depend on derivatives of the measured wave shape—two of them for κ—so clean and accurate data is essential for meaningful results. Achieving this goal also requires that initial conditions be carefully controlled. In particular, 1) the initial temperature and density of the explosive must be uniform and precisely known, 2) the mechanical tolerances must be tight, 3) the confinement (if a "bare" charge is desired) must be sufficiently small, 4) the charge must be long enough that the wave is steady, and 5) thermal expansion or contraction must be accommodated and measured.

Material

The PBX 9502 was Lot# HOL88H891-008, with measured composition 95.00 wt.% TATB / 5.00 wt.% Kel-F 800. Sieve analysis showed 74.8 wt.% $< 45\,\mu$m and 31.2 wt.% $< 20\,\mu$m. The BET surface area was 6236 cm^2/g. The charges were isostatically pressed to 1.890 ± 0.005 g/cm^3.

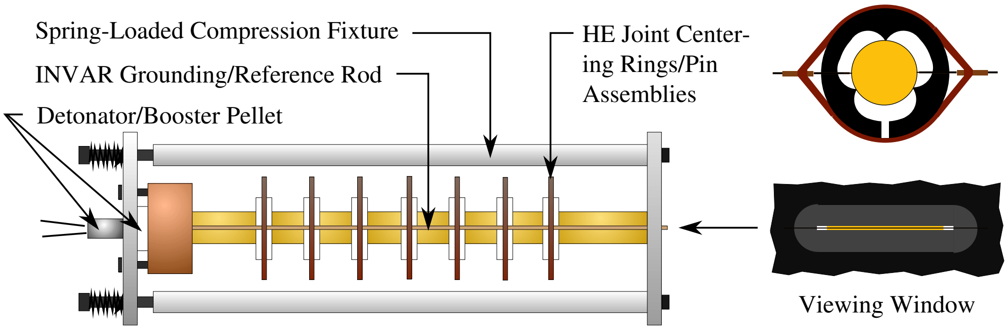

FIGURE 1: RATE STICK DESIGN FOR A WIDE TEMPERATURE RANGE.

Shot Design

The shot assembly is illustrated schematically in Fig. 1. All charges were composed of 50 mm-long segments, as it is impractical to press and machine the entire charge in a single piece. The aspect ratio of the charge assemblies was therefore different for each diameter; the smallest being 13 and the largest 25. All pieces were cored from larger isostatically pressed billets, then finish-machined to ± 0.02 mm. The observation end of the final charge was wet-polished in a close fitting collar on a granite table using fiber optic polishing paper. With PBX 9502 this procedure gives a reasonably specular surface.

Charge segments were held together in a spring-loaded assembly without glue. Segments were laterally located with respect to one another by split rings that contacted the explosive at three points. The rings were made of acetal plastic, and were designed such that they must be spread slightly to fit over the explosive. In this way they applied a radial spring force to mutually locate adjacent segments.

The split rings also provided location for the electrical pins that measured detonation velocity. Each ring held two opposing pins that passed freely through diametrically-drilled holes, and which were spring-loaded against the charge by a silicone O-ring stretched around the periphery. Having two sets of pins offered redundancy, and also allowed measurement of one component of wave tilt. The pin-tips penetrated the surface slightly so as to maintain their Lagrangian position as the charge expanded or contracted. The electrical ground was provided by an INVAR^{TM} (a low expansion alloy) rod running parallel to the charge about 1 cm away. (It is not necessary for the rod to touch the charge, as the electrically-conducting detonation products complete the circuit.) This rod was also used to measure axial thermal expansion—as will be discussed.

The charge assembly was spring-loaded between two aluminum plates. The plate on the detonator end held an SE-1 detonator, which lit a PBX 9501 (95 wt.% HMX) booster pellet captive within a polysulfone housing attached to the plate. The observation end-plate pushed against the main charge and centered it using three small steel dowel pins. Tygon Microbore^{TM} tubing pressed over each dowel pin provided a small cushion that allowed lateral thermal expansion/contraction. The observation window was a slit milled in the plate across the center of the charge. The outside surface of the end-plate was painted flat black to provide two high-contrast edges between which the camera slit was centered.

Temperature Control

The shot box was a polystyrene foam block with a hole bored though the center to contain the experiment. The hole was lined with four wraps of an aluminum-clad polyethylene-foam blanket. This caused much more heat to flow axially (through the aluminum layers) than radially, so that the inner surface was nearly isothermal. The shot was suspended by mounting feet that minimized its contact with the wall. The temperature was controlled by forced air, or by dry nitrogen for cold shots: a swirling flow entered tangentially at the detonator end, and exited tangentially at the observation end. The charge was viewed through two panes of anti-reflection-coated optical glass which, being downstream of the shot, minimized heat loss from it.

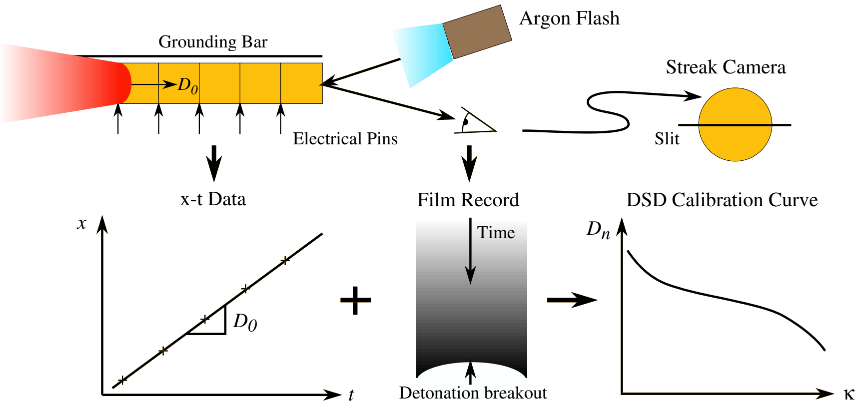

FIGURE 2: SCHEMATIC DIAGRAM OF EXPERIMENT.

Hot shots used an industrial heat gun in which the heating coils were controlled by a PID temperature controller. The control sensor was a type-T thermocouple located on the inflow. A platinum RTD probe accurate to 0.01 C was placed next to it. The temperature was ramped at a rate between 0.5 and 2 C/min depending on charge diameter. When the inflow stabilized at the shot temperature (75 C) the RTD probe was used to apply an offset to the set point. The shots were soaked at temperature between 1 and 4 hours, depending on the charge diameter.

Cold shots used bottled dry nitrogen regulated by a 2 slm mass flow controller. This flow was bubbled through a liquid nitrogen Dewar, and the resulting cold flow was heated to the set temperature by an in-line flow heater. This allowed the temperature to be ramped from ambient to the shot temperature (-55 C) as for the hot shots. It was necessary to introduce a small flow of dry nitrogen between the windows and over the outside window to prevent condensation. Ambient temperature shots were controlled like the hot, with the addition of a steady cold nitrogen offset flow.

During ramping, the outflow temperature lags the inflow temperature due to heat absorption by the shot. During soaking the outflow approaches an equilibrium temperature below that of the inflow, due to steady-state heat losses to the surroundings. A *steady-state* outflow temperature equal to the inflow value implies that the temperature throughout the interior is uniform. Here, the steady-state drop was generally about 0.2 C.

Thermal Expansion Measurement

The axial thermal charge expansion was measured with respect to the INVAR grounding rod, and a small correction was made for the rod's known expansion. The rod screwed into the polysulfone housing at the detonator end of the main charge, and passed freely through a hole in the observation plate. The movement of the rod with respect to the plate was measured by a dial-indicator gauge—also constructed of INVAR—that located on flats on the rod. The gauge was inserted through a hole (that was otherwise plugged) in the shot box; positive ventilation insured that this procedure had little effect on the inside temperature. To test whether expansion was isotropic a similar gauge, also made of INVAR, was used to measure lateral expansion. A measuring head with a 90^o "V" probed the diameter of the explosive, and a rod passing through the apex was displaced proportionally to the deviation of the charge radius from its ambient value.

Dynamic Measurements

The charge was tilted 10^o to the optical axis, and was illuminated by an argon flash such that specularly reflected light pointed at the camera (see Fig. 2). When the wave breaks out the reflectivity decreases sharply—and virtually instantly—to give a high contrast film record. (PBX 9502 reaction gives much less light than the flash.) The pin circuits were powered by Los Alamos DM-11 boards, in which each pin closure fires an RC circuit, producing a short voltage pulse. These are multiplexed to one signal cable.

ANALYSIS

The front-curvature data was read on an optical comparator, using a data acquisition program that incremented the radius such that the arc length between points was approximately constant. This reduced sparsing of the points near the edges where the function changes fast. The magnification was determined directly from the edges of the dynamic record. This, together with the camera writing speed, determined the breakout time t as a function of the radius r.

The $x-t$ pin data was fit with a least squares line to determine the axial detonation velocity D_0. The average uncertainty in velocity due to random scatter was ± 4.3 m/s. Since the wave is steady, the breakout time $t(r)$ multiplied by D_0 gives the wave shape $z(r)$.

The wave tilt in the slit direction was estimated from separate fits to the left and right sets of pin data. The resulting angle was about 0.1^o, which evidently errs on the high side due to scatter in the $x-t$ data. Apparent tilt may also arise from measurement error in that there is, inevitably, a small amount of play in the camera mirror bearings. This causes the slit to be out of square, in a small but unpredictable way, with the writing direction. The result is a time error proportional to the radius. We were not equipped to distinguish between the two errors, but it is unnecessary to do so because the same correction is sensible for correcting both types of tilt. To apply an optimal global linear tilt correction one fits a line to the time difference between two sides as a function of radius, and shifts the data antisymmetrically in time according to the line. Corrected in this manner, data scatter from both sides combined was comparable to that for each side alone. The fit was therefore applied to the combined set.

The processed data was fit using the series

$$z(r) = -\sum_{1}^{n} a_n \ln\left[\cos\left(\eta\frac{\pi}{2}\frac{r}{R}\right)\right]^n, \qquad (1)$$

where R is the charge radius and a_n and η are fitting parameters. This form was motivated by Bdzil[2], who showed that for small shock angles $z \propto \ln[J_0(r)]$ (where J_0 is Bessel's function of order zero) gives a linear $D_n(\kappa)$ function in cylindrical geometry. Others (e.g. Forbes and Lemar[3]) later adopted this function as a fitting form. To generate nonlinear $D_n(\kappa)$ curves one may use $\ln[J_0(r)]$ as the basis function in a power series. Alternatively we use $\ln[\cos(r)]$—the analogous result in slab geometry—because it fits the data equally well and is more computationally efficient.

Equation 1 has two desirable properties. First, it yields monotone derivatives, a consequence of the fact that least squares fits almost universally give coefficients a_n of the same sign. (Most series fits, notably polynomials, generate spurious fluctuations in the derivatives.) Second, it can handle the observed rapid curvature changes at the charge edges. The behavior near the edge is controlled by the parameter η (one value for all terms), which controls the position of a singularity in the basis functions outside the fitting domain. For $\eta = 0$ the singularity is at $r = \infty$, for $\eta = 1$ it is at the charge edge. For PBX 9502 three terms generally give the most desirable fits.

A sample data set and the fit to it is shown in Fig. 3. The fit residuals, magnified ten times for clarity, are shown below. The standard deviation of the combined residuals is 4.3 μm (dashed lines). This measure depends on each step of the process—the symmetry and smoothness of detonation, the breakout observation, the camera/film resolution, the film digitization, and the curve fit—and is thus a measure of net accuracy.

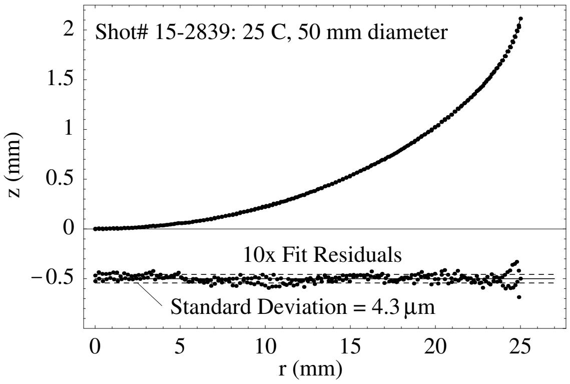

FIGURE 3: WAVE SHAPE DATA, FIT, AND 10-X FIT RESIDUALS FOR A 50 MM DIAMETER 25 C CHARGE. (SHOT# 15-2839)

The $D_n(\kappa)$ curve is obtained from D_0 and the slope $s(r)$ of the wave profile $z(r)$:

$$s(r) \equiv \frac{\mathrm{d}z(r)}{\mathrm{d}r} = \tan\theta(r), \qquad (2)$$

where $\theta(r)$ is the local angle between the charge axis and the direction normal to the wavefront. All generating functions are parametric in r; thus, $D_n(\kappa)$ curves are generated by plotting $D_n(r)$ versus $\kappa(r)$. The normal detonation velocity is $D_0 \cos\theta(r)$, or

$$D_n(r) = \frac{D_0}{\sqrt{1+s(r)^2}}. \qquad (3)$$

The total curvature is the sum of two terms. The first is that of the curve defined by the intersection of the wavefront with a plane through the axis (i.e., Fig. 3); this is the familiar formula from plane geometry. The second describes the additional curvature arising from axial symmetry:

$$\kappa(r) = \frac{s'(r)}{[1+s(r)^2]^{\frac{3}{2}}} + \frac{s(r)}{r\sqrt{1+s(r)^2}}. \qquad (4)$$

One can readily show that these two terms are equal on the axis, as is required by symmetry.

Other quantities that arise in higher order DSD formulations can be generated in an analogous manner. For example $\dot{D}_n(r)$, the acceleration of the wavefront normal to itself, is given by:

$$\dot{D}_n(r) = -\frac{D_0^2 s(r)^2 s'(r)}{[1+s(r)^2]^{\frac{5}{2}}}. \qquad (5)$$

When substituted into Eq. 1 the above equations, though analytic, are sufficiently lengthy so as to require symbolic manipulation. The present calculations were performed in *Mathematica.*

Concealed within this ostensibly robust, explicit formulation is an important practical difficulty. The optical record should terminate at a sharp point as shown in Fig. 2, but in reality this point is slightly blunted by the finite resolution of the camera and film. The effect on the digitized data is that the last point is not real, but is extrapolated from neighboring points. This poses no problem in determining the wave shape since the extrapolation distance is small. Unfortunately, the curvature changes so fast near the edge that the consequence in $D_n(\kappa)$ space may be substantial. It is clear that this lack of resolution causes one to underestimate the true edge curvature, but it is impossible to say by how much.

When measurements break down one must appeal to theory for guiding restrictions. While theory provides no constraint on the edge curvature κ_e, it does predict the edge angle θ_e to within several degrees. Comparing the theoretical angles estimated by Bdzil[4] with those determined directly from data fits, we find that the measured edge angles are close to 30^o, while the calculated angles are in the low 40's. We then examined whether the fit qualities would suffer if a 40^o angle were imposed as a constraint—and found that they were virtually unaffected. Hence the present measurements are compatible with theoretical edge angles but are unable to predict them.

Constraining θ_e does not uniquely determine κ_e (since the latter also depends on $s'(r)$), but does have a strong influence on it. The sensitivity of κ_e to an imposed edge angle is illustrated in Fig. 4, which shows three $\kappa(r)$ curves generated from fits to the data of Fig. 3, with imposed edge angles of 30^o, 40^o, and 50^o. All three fits are of similar quality. Remarkably, each curve looks to be exponentially increasing in semi-log space, in which exponential curves are *linear.* The curvature near the edge changes rapidly indeed.

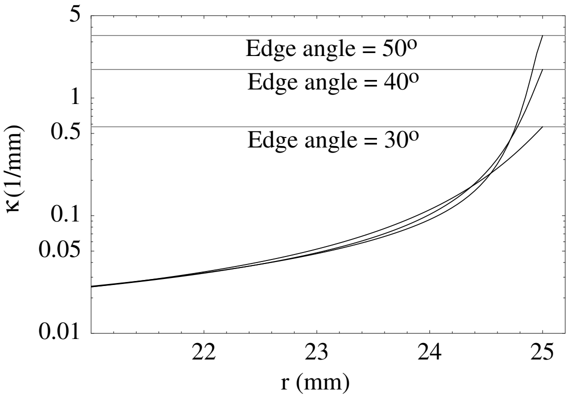

FIGURE 4: $\kappa(r)$ CURVES FOR FITS TO THE DATA OF FIG. 3, WITH DIFFERING EDGE ANGLE CONSTRAINTS.

Figure 4 shows that differing edge angle constraints have a substantial influence only within about 2% of the edge, but in that region the three curves diverge significantly: κ_e differs by a factor of six between the 30^o and 50^o cases. This exercise demonstrates the necessity (but not the sufficiency) of constraining θ_e in fitting the present data. Accordingly, the subsequent results impose an edge angle of 40^o. Having done so the remaining uncertainty in κ_e (given a fitting form) is tied to the uncertainty in placing the last data point.

RESULTS

Thermal Expansion

When tested on inert reference materials, the thermal expansion gauges reproduced handbook values. The same measurements performed on PBX 9502 were somewhat erratic: a problem also experienced by Campbell[5]. Nevertheless, expansion was consistently *anisotropic*. In light of these two observations the axial and radial data for each temperature were separately averaged. Because the measurement resolution scaled with stick size, the averages were weighted in proportion to the stick length for axial measurements, and according to the diameter for radial measurements. Results are given in Table 1 along with the volumetric coefficient ($\alpha_V = \alpha_A + 2\alpha_R$ for a cylinder), the nominal linear coefficient ($\alpha_L = \alpha_V/3$), and Campbell's average axial coefficient. The present axial coefficients are greater than Campbell's, and the present radial coefficients are less.

TABLE 1: MEAN COEFFICIENTS OF THERMAL EXPANSION ($C^{-1} \times 10^5$)

Type	Symbol	Cold (-55 C)	Hot (75 C)
Axial	α_A	6.4	12.5
Radial	α_R	3.9	6.8
Volumetric	α_V	14.2	26.1
Nominal Linear	α_L	4.7	8.7
Axial (Ref. 5)	α_A	5.6	7.9

That isostatically pressed charges can expand anisotropically is surely a consequence of the fact that individual TATB crystals do so.[6] However, since the grain orientation in PBX 9502 molding powder is random, one expects anisotropy on the grain scale to average out over many particles. If the initial random orientation was maintained during pressing, the bulk expansion of the finished piece would remain isotropic. The fact that it is not suggests that crystals do in fact assume a preferred orientation while compacting.

For isostatic pressings the culprit cannot be wall friction, but rather that mass elements flow in a particular direction through a displacement while compacting—regardless of how material is consolidated. Furthermore, the displacement history of mass elements varies throughout a charge. For isostatic pressing the maximum displacement occurs at the edges, and there are symmetry points or planes where none occurs. Thus it is not surprising that, when samples are cored from different parts of a billet and assembled at random, the results are somewhat erratic.

Detonation Velocity and Wave Shape

Three charge sizes were fired at each initial temperature T_0: 50 mm, 18 mm, and 8, 10, and 12 mm respectively for the 75 C, 25 C, and -55 C cases. Each small diameter was slightly larger than the failure diameter at its T_0.[5] Table 2 gives the detonation velocity and wave shape fits (valid for $0 \leq r \leq R$). Charge dimensions at T_0 are determined from Table 1: charge radii use α_R, detonation velocities use α_A, and densities (the average value for all pinned segments) use α_V.

Our values of D_0 for the three 50 mm charges are ≈0.5% below Campbell's[5]; this appears consistent with lot variations and the fact that our 50 mm charges were toward the low end of the density tolerance. For our three small sticks the deviation from Ref. 5 remains 0.5% at 75 C, is 0.65% at 25 C, and 0.8% at -55 C. That the discrepancy decreases with temperature suggests that Campbell's lot was more sensitive than ours. This interpretation is consistent with the fact that his lot (#79-04) had 4.5 times the BET surface area. Experience with granular explosives—including TATB[7]—is that finer-grained explosives are more sensitive at high pressures.

The wave shapes given in Table 2 are plotted in Fig. 5. For each charge diameter hotter waves are slightly flatter because (due to highly temperature-sensitive kinetics) they have thinner reaction zones. Since the smallest three sticks have different diameters, their order is reversed.

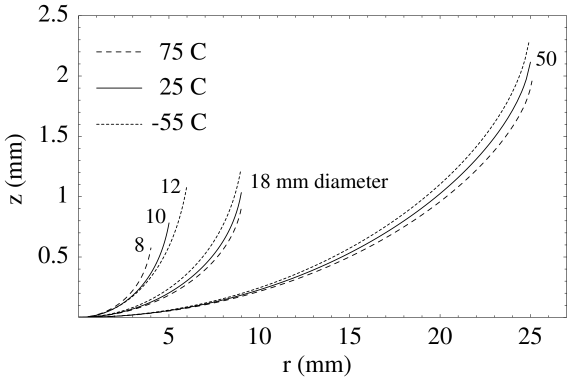

FIGURE 5: FITS TO WAVEFRONT DATA.

TABLE 2: DIAMETER EFFECT DATA AND WAVEFRONT FITS

Shot Number	Initial Temp. T_0 (C)	Average Density $\rho(T_0)$ (g/cc)	Charge Radius R (mm)	Detonation Velocity D_0 (mm/μs)	Fitting Parameter a_1 (mm)	Fitting Parameter a_2 (mm)	Fitting Parameter a_3 (mm)	Fitting Parameter η
15-2853	-55.0	1.912	5.980	7.392	0.588788	0.060233	0.000000	0.944751
15-2849	-55.0	1.914	8.975	7.497	0.605798	0.083354	0.004114	0.974357
15-2842	-55.0	1.915	24.930	7.636	1.239912	0.258651	0.024484	0.984395
15-2851	25.0	1.890	5.005	7.415	0.405904	0.045971	0.001651	0.954741
15-2844	25.0	1.886	9.005	7.523	0.527673	0.089709	0.008939	0.970535
15-2839	25.0	1.886	25.000	7.641	1.151004	0.240261	0.021081	0.988622
15-2852	75.0	1.866	4.005	7.400	0.294247	0.036272	0.002635	0.955363
15-2843	75.0	1.862	9.035	7.506	0.479014	0.089606	0.008808	0.977421
15-2841	75.0	1.862	25.085	7.616	1.090885	0.235300	0.020671	0.990250

$D_n(\kappa)$ Curves

The $D_n(\kappa)$ curves for the Table 2 fits are graphed in Fig. 6. For each T_0, curves for different charge diameters follow nearly a common path for $\kappa \leq 0.1$ mm^{-1}, a value that corresponds to a 40 mm diameter spherical wave. For larger κ the curves progressively diverge, those for larger sticks lying above the smaller, in agreement with our numerical simulations.[8] That the edge curvature κ_e increases with diameter contradicts the same calculations; in fact, neither the experiment nor the numerics resolve κ_e. The gray dot on the 50 mm, 25 C curve corresponds to $0.98R$: the approximate point (see Fig. 4) at which κ begins to be strongly influenced by the imposed edge angle.

The normal velocity at the edge is given by $D_{ne} = D_0 \cos\theta_e$. D_0 is accurately measured; θ_e can be calculated to perhaps $\pm$ 5^o and is fixed (somewhat arbitrarily) at 40^o. This constraint and the observation that D_0 changes only modestly with size and temperature mean that the predicted value of D_{ne} (in contrast to κ_e) is almost constant. Note that because θ_e is prescribed, D_{ne} is independent of the data fit.

Curves for different charge diameters at the same temperature come together asymptotically at small curvature, but curves for different temperatures at the same diameter cross each other in the region $0.05 < \kappa < 0.1$ mm^{-1}. Crossing occurs due to two competing phenomena. For plane waves the primary temperature effect is thermal expansion: colder charges are denser and the wave travels faster. For curved waves the detonation speed depends on the reaction zone thickness: cold waves have thicker reaction zones and travel slower. Therefore, the $D_n(\kappa)$ curves for charges of equal diameter but different initial temperatures will generally cross somewhere. Being of a generic nature, this behavior should apply to essentially all solid explosives.

Another clear feature of every curve in Fig. 6 is the upward turn at small curvatures. This behavior is also evident in Campbell's [5] diameter effect curves, and at that time was unprecedented. Since then the effect has been seen in other nonideal explosives, and is understood to indicate a slow reaction component that is, to an extent that depends on the wave curvature, decoupled from the detonation shock by the sonic surface.

DSD CALIBRATION SURFACE

The simplest DSD theory predicts a unique $D_n(\kappa)$ function provided that κ is sufficiently small. The present data validates this aspect of the model where that assumption holds, and illustrates the problems (i.e. non-uniqueness) that arise when κ is large. It is nevertheless useful to deduce an optimal calibration over the full range of observed curvatures, understanding that calculations will be most accurate where the model assumptions are best satisfied.

The strategy is to choose a flexible, empirical analytic form with the correct qualitative shape, and enough parameters to span the range of observed behavior. This equation is used to generate wave shapes and a diameter effect curve that are compared to the corresponding data. The $D_n(\kappa)$ parameters are globally optimized (within the limits of user-defined weighting parameters) using a nonlinear least-squares solver. Performing the procedure for each temperature gives three values for each coefficient, parabolic fits to which give a smooth surface $D_n(\kappa, T_0)$ that passes exactly through the three $D_n(\kappa)$ curves.

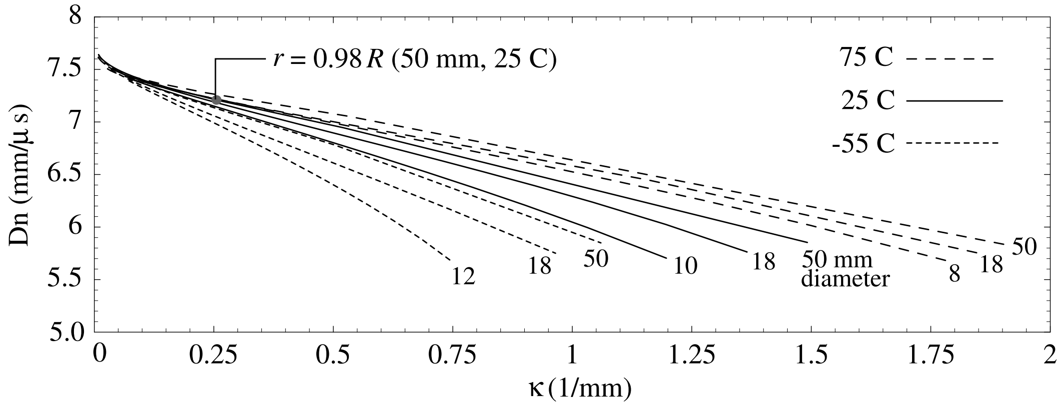

FIGURE 6: $D_n(\kappa)$ CURVES.

Our equation for $D_n(\kappa)$ is:

$$\frac{D_n(\kappa)}{D_{cj}} = 1 + A\left[(\kappa_f - \kappa)^\alpha - \kappa_f^\alpha\right] - \frac{B\kappa^\beta}{1 + C\kappa^\gamma} \quad (6)$$

where κ_f (the failure curvature), D_{cj} (the plane wave velocity), A, B, C, α, β, and γ are fitting parameters. The edge angle is constrained to 40^o as before. The shock fits generated by optimal fits of Eq. 6 are all excellent to about 90% of the stick radius, but tend to diverge in a layer near the edge. This is expected, since it has already been shown that a single $D_n(\kappa)$ function cannot fit all the high-curvature data simultaneously. The resulting surface is shown in Fig. 7, the fitting parameters for which are listed in Table 3. The dominant feature of the surface is the dramatic increase of κ_f with temperature.

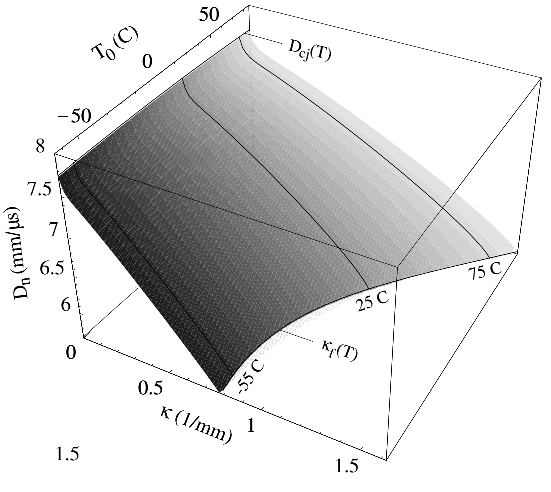

FIGURE 7: DSD CALIBRATION SURFACE.

CONCLUSIONS

We confirm the expectation that, for a given diameter, waves in hotter charges are slightly flatter than those in colder ones. Moreover, $D_n(\kappa)$ curves for hotter charges cross those for colder ones, D_n for hotter charges being slower for small κ and faster for large κ.

For a given T_0, different charge sizes trace a common $D_n(\kappa)$ curve for small κ (which, owing to a long reaction tail, is also concave up there) but diverge and become concave down as κ increases. $D_n(\kappa)$ curves for larger sticks lie above, and span both smaller and larger κ, than do curves for smaller ones. The latter result is uncertain due to poor accuracy at large κ, and is contradicted by numerical simulations. The largest κ_e (50 mm, 75 C case) was about 2.5 times the smallest (12 mm, -55 C case), but D_{ne} was almost constant.

An optimal $D_n(\kappa)$ calibration is determined from -55 C to 75 C, and is expressed as a smooth $D_n(\kappa, T_0)$ surface. The effect of T_0 is minimal at low κ but substantial at high κ.

TABLE 3: FITTING PARAMETERS FOR $D_n(\kappa, T_0)$, -55 $\leq T_0$ (C) $\leq$ 75 (USE IN EQ. 6).

Par.	1	T_0 (C)	${T_0}^2$
D_{cj}	7.73839E0	-3.02535E-4	-6.16034E-6
κ_f	9.17958E-1	4.76714E-3	4.15663E-5
A	2.73487E-1	-1.08683E-3	-1.60866E-6
B	3.25898E-1	1.71067E-4	-1.05764E-6
C	4.26638E1	-2.94613E-1	1.56457E-3
α	8.50096E-1	-1.06919E-3	7.63033E-6
β	6.91904E-1	4.76804E-4	4.79015E-6
γ	1.22377E0	-5.06637E-4	1.08957E-5

ACKNOWLEDGEMENTS

We thank Phil Howe for initiating and funding this project, Bill Davis and Bob Critchfield for technical advice, Howard Stacy for instrumentation help, Don Murk and Bert Harry for help assembling and firing the shots. This work was supported by the U.S. Department of Energy.

REFERENCES

1. Aslam, T.D.; Bdzil, J.B; and Stewart, D.S. Level Set Methods Applied to Modeling Detonation Shock Dynamics. *J. Comp. Phys.* vol. 120, pp. 390-409, 1996.

2. Bdzil, J.B. Steady-State Two-Dimensional Detonation, *J. Fluid Mech.*, vol. 108, pp. 195-226, 1981.

3. Forbes, J.W.; and Lemar, E.R. Detonation Wave Velocity and Curvature of a Plastic-Bonded, Nonideal Explosive PBXN-111 as a Function of Diameter and Confinement, *J. Appl. Phys.*, vol. 84 no. 12, 1998.

4. Bdzil, J.B. Unpublished Calculations.

5. Campbell, A.W. Diameter Effect and Failure Diameter of a TATB-Based Explosive, *Prop., Expl., Pyro.* vol. 9, pp. 183-187, 1984.

6. Kolb, J.R.; and Rizzo, H.F. Growth of 1,3,5-Triamino-2,4,6-TrinitroBenzene (TATB) I. Anisotropic Thermal Expansion, *Prop., Expl., Pyro.*, vol. 4, pp. 10-16, 1979.

7. Lee, K.-Y.; Kennedy, J.E.; Hill, L.G.; Spontarelli, T.; Stine, J.R.; and Kerley, G. Synthesis, Detonation Spreading, & Reaction Rate Modeling of Fine TATB, These Proceedings.

8. Aslam, T.D.; Bdzil, J.B.; and Hill, L.G. Extensions to DSD Theory: Analysis of PBX 9502 Rate Stick Data, These Proceedings.

DISCUSSION

Yehuda Partom
RAFAEL
Box 2250, Haifa 31021, ISRAEL

Regarding the problem of recording the detonation front at the charge edge as you've indicated: running a 2D hydro-reactive code we see that the reaction front stays away from the boundary by a distance of order the reaction zone thickness. Other workers have seen this too—even in this symposium. Maybe this is the reason for the problem of recording the front at the boundary.

REPLY BY L.G. HILL

We believe that the high shock-curvatures observed near the charge edge are associated with weaker—but finite—reaction there. This notion is supported by Aslam's well-resolved direct numerical simulations. Consider the following example using PBX 9502-like parameters and a pressure dependant reaction rate law $\dot{\lambda} \propto p^2\sqrt{1-\lambda}$, where λ is the mass fraction reacted. There are 128 cells across a 1D reaction zone; for details about the numerical method see Ref. 8.

Figure 8 gives results in a coordinate system normalized by the 1D reaction zone length δ. Three values of $\dot{\lambda}$ at the shock, normalized by the center line value, are also indicated. Note that $\dot{\lambda}$ at the edge is a substantial 46% of the center line value. This alone does not guarantee a large accumulation of product near the edge since, after passing through the shock, material there immediately experiences a large pressure drop (accompanied by a decrease in $\dot{\lambda}$) through the reflected expansion fan. Consequently the λ-values attained near the boundary depend on both the confinement and the reaction rate law. In this instance, the $\lambda = 0.15$ contour meets the material boundary at about a distance δ from the shock.

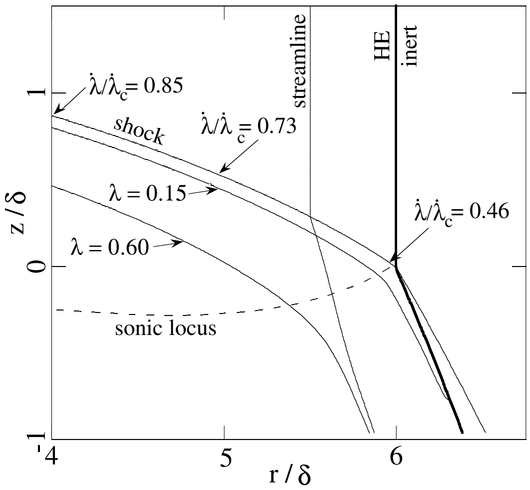

FIGURE 8: DIRECT NUMERICAL SIMULATION OF A PBX 9502-LIKE RATE STICK.